

Experimental observation of non-Abelian topological charges and edge states

<https://doi.org/10.1038/s41586-021-03521-3>

Received: 1 October 2020

Accepted: 6 April 2021

Published online: 9 June 2021

 Check for updates

Qinghua Guo^{1,9}, Tianshu Jiang^{1,9}, Ruo-Yang Zhang^{1,9}, Lei Zhang^{1,2,3}, Zhao-Qing Zhang¹, Biao Yang^{1,4,5} , Shuang Zhang^{6,7,8}  & C. T. Chan¹ 

In the last few decades, topological phase^{1–11} has emerged as a new classification of matter states beyond the Ginzburg–Landau symmetry-breaking paradigm. The underlying global invariant is usually well characterized by integers, such as Chern numbers or winding numbers—the Abelian charges^{12–15}. Very recently, researchers proposed the notion of non-Abelian topological charges^{16–19}, which possess non-commutative and fruitful braiding structures with multiple (more than one) bandgaps tangled together. Here we experimentally observe the non-Abelian topological charges in a time-reversal and inversion-symmetric transmission line network. The quaternion-valued non-Abelian topological charges are clearly mapped onto an eigenstate-frame sphere. Moreover, we find a non-Abelian quotient relation that provides a global perspective on the distribution of edge/domain-wall states. Our work opens the door towards characterization and manipulation of non-Abelian topological charges, which may lead to interesting observables such as trajectory-dependent Dirac/Weyl node collisions in two-dimensional systems^{16,17,20}, admissible nodal line configurations in three dimensions^{16,19,20}, and may provide insight into certain strongly correlated phases of twisted bilayer graphene²¹.

Topological band theory describes the global topological phases underlying various physical systems. Previously, topological phases are classified into \mathbb{Z} or \mathbb{Z}_2 classes, which are the Abelian groups. They are commutative and exhibit additive properties. The induced bulk–edge correspondence^{1,22–24} also inherits the Abelian nature, with the number of domain-wall states being the difference between the two topological invariants across the domain wall. Very recently, it is found that symmetry-protected topological phases can go beyond the Abelian classifications. With multiple bandgaps tangled together, the underlying topological invariants are represented by non-Abelian groups^{16–19}, which reveal the underlying braiding topological structures.

However, so far, the experimental observation of non-Abelian topological charges describing band braiding remains elusive. Here we experimentally demonstrate a three-band PT (inversion and time-reversal) symmetric system and characterize the underlying non-Abelian topological charges in the momentum space. We further investigate the edge/domain-wall states, and show that their detailed configurations cannot be entirely explained by the conventional bulk–edge correspondence.

Non-Abelian topological charges

We start with a mathematical model to experimentally illustrate the non-Abelian topological charges. Usually, the combination of P and

T operators can be represented by complex conjugation K when a suitable basis is chosen²⁵. Under PT symmetry, the Hamiltonian is hence real at all momenta k , that is, $H(k) = H^*(k)$, where the asterisk denotes the complex conjugate. Without loss of generality, a three-band Hamiltonian with two complete bandgaps takes the form of $H(k) = \sum_{n=1}^3 n|u_k^n\rangle\langle u_k^n|$ where $|u_k^n\rangle$ is a real three-dimensional vector. The corresponding order-parameter space of the Hamiltonian is then $M_3 = O(3)/O(1)^3$, where $O(N)$ is the orthogonal group (see details in Supplementary Information section I and Supplementary Figs. 1, 2). The fundamental homotopy group of the system can be expressed as $\pi_1(M_3) = \mathbb{Q}$, where $\mathbb{Q} = (+1, \pm i, \pm k, -1)$ forms the non-Abelian quaternion group^{16,26,27}, consisting of three anti-commuting imaginary units satisfying $ij = k$, $jk = i$, $ki = j$ and $i^2 = j^2 = k^2 = -1$. Figure 1a pictorially illustrates all the elements of \mathbb{Q} and their group multiplications are represented via coloured arrows.

For simplicity, we assume the initial eigenstates of the Hamiltonian are three orthogonal vectors, $H\mathbf{x} = 1\mathbf{x}$, $H\mathbf{y} = 2\mathbf{y}$ and $H\mathbf{z} = 3\mathbf{z}$, which form a right-handed Cartesian coordinate frame. The ‘toy’ Hamiltonian can then be expressed as, $H(k) = R(k)\text{diag}(1, 2, 3)R(k)^\top$ with $R(k) = \exp[\boldsymbol{\beta}(k) \cdot \mathbf{L}]$, where $(L_i)_{jk} = -\epsilon_{ijk}$, ϵ_{ijk} is the fully antisymmetric tensor, and $\boldsymbol{\beta}(k) = \phi\mathbf{n}$ is the product of the rotation axis $\mathbf{n}(k)$ and rotation angle $\phi(k)$ (see Supplementary Information section I). The one-dimensional (1D) systems with quaternion charges of $+i$, $+j$, $+k$, are realized via $R(k) = \exp[(k + \pi)L_{x,y,z}/2]$, respectively. The case of $+i$ is shown in Fig. 1b, where the eigenstate frame rotates $\phi = \pi$ around the x axis. The inset of Fig. 1b shows three

¹Department of Physics and Institute for Advanced Study, The Hong Kong University of Science and Technology, Hong Kong, China. ²State Key Laboratory of Quantum Optics and Quantum Optics Devices, Institute of Laser Spectroscopy, Shanxi University, Taiyuan, China. ³Collaborative Innovation Center of Extreme Optics, Shanxi University, Taiyuan, China. ⁴College of Advanced Interdisciplinary Studies, National University of Defense Technology, Changsha, China. ⁵Hunan Provincial Key Laboratory of Novel Nano-Optoelectronic Information Materials and Devices, National University of Defense Technology, Changsha, China. ⁶School of Physics and Astronomy, University of Birmingham, Birmingham, UK. ⁷Department of Physics, The University of Hong Kong, Hong Kong, China. ⁸Department of Electrical and Electronic Engineering, The University of Hong Kong, Hong Kong, China. ⁹These authors contributed equally: Qinghua Guo, Tianshu Jiang, Ruo-Yang Zhang.  e-mail: yangbiaocam@nudt.edu.cn; shuzhang@hku.hk; phchan@ust.hk

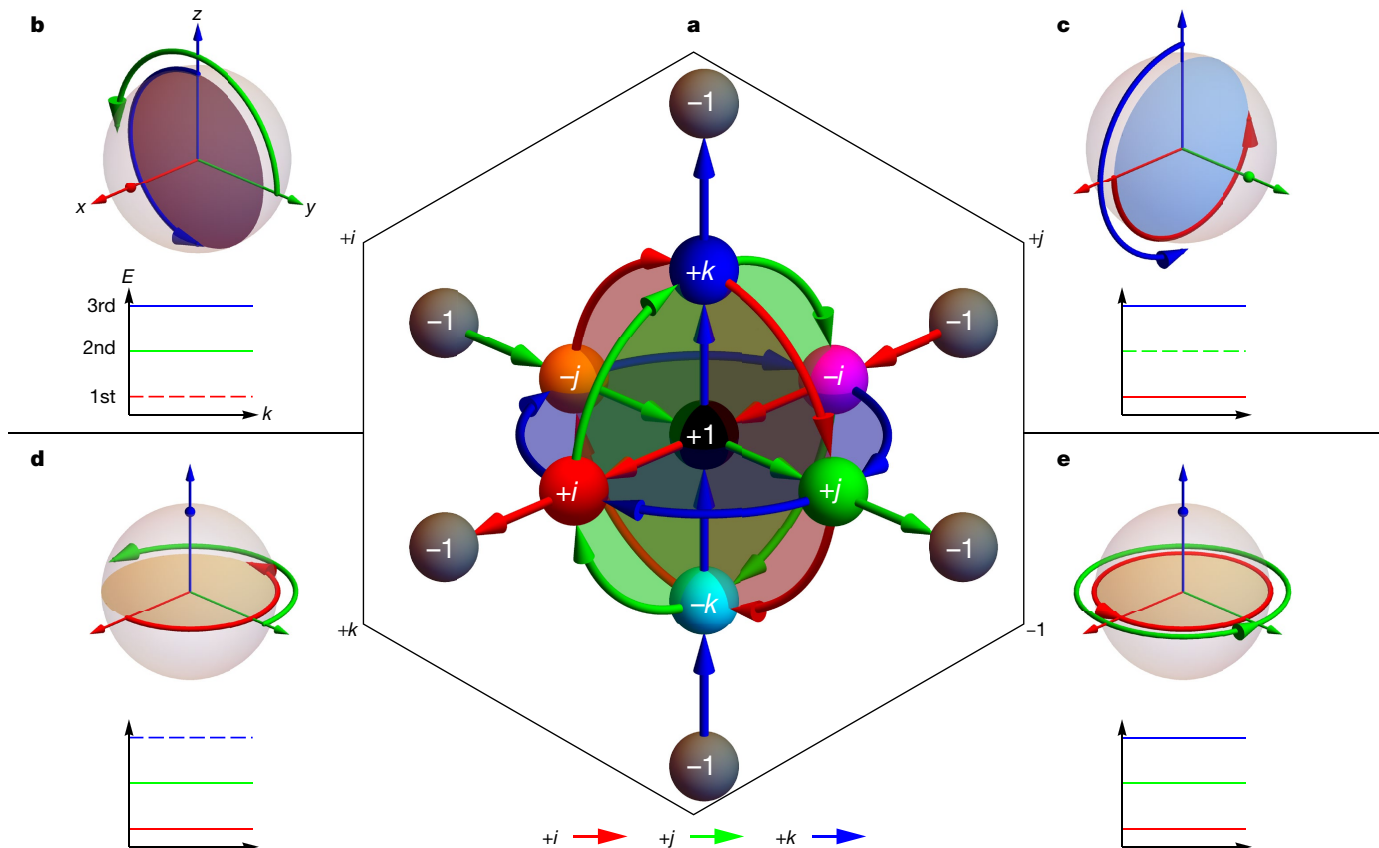


Fig. 1 | Non-Abelian topological charges. **a**, Graphical representation of the quaternion group \mathbb{Q} and associated non-Abelian structures. The elements are indicated by spheres, with coloured arrows defining their mutual multiplications. Each red, green and blue arrow represents multiplication by $+i$, $+j$ and $+k$, respectively, for example, $i \cdot (red \rightarrow) = i^2 = -1$, whereas its reverse direction means multiplying by the corresponding conjugation partner $-i$, $-j$ or $-k$. **b**, Rotation of the eigenstate frame around the x -axis through an angle

of π induces the non-Abelian topological charge of $+i$. The eigenstate (red dot) of the first band (red dashed line in inset) remains fixed. **c, d**, Similar to **b** with respect to the non-Abelian topological charges $+j$ (**c**) and $+k$ (**d**). **e**, Rotation of eigenstate frame around the z -axis through 2π induces the non-Abelian topological charge of -1 . Red, green and blue colours indicate the real eigenstate trajectory of the first, second and third bands, respectively. The arrow indicates the direction when k runs from $-\pi$ to π across the first Brillouin zone.

non-degenerate flatbands with the trivial band (the first band) marked by dashed line. Similarly, the other two non-Abelian topological charges $+j$ and $+k$ are given in Fig. 1c, d, where the eigenstate frames rotate $\phi = \pi$ around the y or z axes, resulting in the second or third bands being trivial, respectively. The conjugate partners $-i$, $-j$ and $-k$ correspond to the inverse rotations. It is worth emphasizing that two conjugate elements (for example, $\pm i$) can only be well defined when they share a common basepoint¹⁶. From these insets, one can see that the non-Abelian topological phase transitions require band re-ordering, such as the dashed band jumping up (down) when the charge alters from $+j$ to $+k$ ($+i$). The process inevitably encounters gap closing and reopening (see Supplementary Information section IV and Supplementary Figs. 8–10).

The unit element $+1$ represents the trivial case, where the trajectories of the three-eigenstates can be continuously contractible to three isolated points $(1, 0, 0)$, $(0, 1, 0)$ and $(0, 0, 1)$ (see Supplementary Information section II and Supplementary Fig. 3g). This is very different from the nontrivial case of charge -1 illustrated by Fig. 1e. Taking $R(k) = \exp[(k + \pi)L_{x,y,z}]$, the Hamiltonian carries charge of -1 , corresponding to rotating the eigenstate frame through an angle $\phi = 2\pi$ around the x , y , or z axes, respectively. One can smoothly transform $R(k)$ between these three cases without closing the bandgaps (see Supplementary Information section V, Supplementary Fig. 11), and as such they are classified as the same topological phase.

Tight-binding model

We consider a quasi-1D system with three meta-atoms (A, B, C) per unit cell, with inter-cell couplings indicated in Fig. 2a. The real-space

Hamiltonian reads (see Supplementary Information section III for more general cases, Supplementary Fig. 4),

$$\mathcal{H} = \sum_n \left(\sum_{X=A,B,C} s_{XX} c_{X,n}^\dagger c_{X,n} + \sum_{\substack{X=A,B,C \\ Y=A,B,C}} v_{XY} c_{X,n}^\dagger c_{Y,n+1} + \text{h.c.} \right), \quad (1)$$

where $c_{X,n}^\dagger$ and $c_{X,n}$ denote the creation and annihilation operators, respectively, on the sublattices X or Y and at site n . After Fourier transformation, we obtain

$$H(k) = \begin{bmatrix} s_{AA} + 2v_{AA} \cos k & 2u \sin k & 2w \sin k \\ 2u \sin k & s_{BB} + 2v_{BB} \cos k & 2v \sin k \\ 2w \sin k & 2v \sin k & s_{CC} + 2v_{CC} \cos k \end{bmatrix}, \quad (2)$$

where we have set $v_{AB} = v_{BA} = iu$, $v_{BC} = v_{CB} = iv$ and $v_{CA} = v_{AC} = iw$ to make the Bloch Hamiltonian explicitly real (u , v and w are all real). The tight-binding model constructed here is PT symmetric, despite the fact that it breaks both time-reversal and inversion symmetries. We first choose parameters (Supplementary Table 1) that can mimic the flatband cases as shown in Fig. 1b–e (note that Fig. 1e requires next-nearest-neighbour hoppings, see Supplementary Information section III).

Figure 2b–e presents the edge states localized at the hard boundaries of the quasi-1D lattices with different values of non-Abelian topological

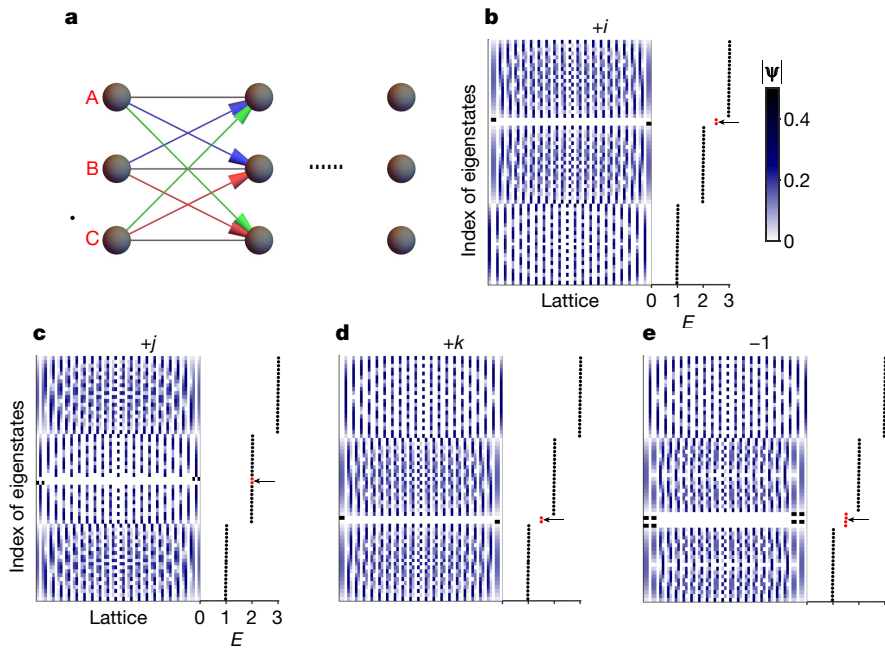


Fig. 2 | Realizing non-Abelian topological charges in a tight-binding model.

a, Schematic view of the tight-binding configuration, where only the nearest-neighbour hoppings are considered. The directional hoppings are $v_{AB} = v_{BA} = iu$ (blue), $v_{BC} = v_{CB} = iv$ (red) and $v_{CA} = v_{AC} = iw$ (green). **b–e**, Edge states (red dots) at hard boundaries for systems with charges of $+i$ (**b**), $+j$ (**c**), $+k$ (**d**) and -1 (**e**). The normalized eigenstate distributions ($|\Psi|$, in arbitrary units) as a function of lattice position (left panels) are illustrated, accompanied by the

eigenenergy profiles (right panels). A tiny modulation (1%) is imposed on v_{XX} ($X = A, B, C$) to avoid a huge degeneracy. The quasi-1D lattice has 21 periods here. The case of **b** with a non-Abelian charge of $+i$ can be realized by setting $s_{AA} = 1$, $s_{BB} = s_{CC} = 5/2$, $v_{BB} = -v_{CC} = 1/4$ and $\nu = 1/4$ (the other parameters are zero unless otherwise specified). The parameters for the other cases (**c–e**) are shown in Supplementary Table 1 (see Supplementary Information section III).

charges¹⁶. The usual Abelian topological charges are used to characterize the topology of a single bandgap, the value of which counts the number of edge states inside that bandgap. However, from the non-Abelian perspective, the non-Abelian charges describe the topology of all bandgaps, and can hence predict both the distribution and number of edge states in all bandgaps. As shown in Fig. 2b, the charge of $+i$ indicates the second gap is nontrivial and supports one edge state on each end of a finite-length lattice. The eigenstate of the first band is fixed, whereas the eigenstates of the second and third bands rotate through π for k running from $-\pi$ to $+\pi$, and the bandgap sandwiched by these two rotating states carries edge states. Similar arguments also apply to charges of $+j$ and $+k$, as shown in Fig. 2c, d, respectively. It is interesting to note from Fig. 2c for a charge of $+j$ that the edge states merge into the second continuum band, forming bound-states-in-continuum (BICs). It is worth emphasizing that the BICs are not enforced by the non-Abelian topology but accidentally achieved by pertaining to some specific parameters. By contrast, the quaternion charge of -1 supports two edge states on each edge as shown in Fig. 2e. Nevertheless, the locations of the edge states of charge -1 are fickle and can vary according to the details of bulk states¹⁶ (Supplementary Fig. 11, see details in Supplementary Information section V).

Braiding network realization

In the experiment, a network consisting of 13 periods was designed to characterize the non-Abelian topological charges. There are three meta-atoms A, B and C in one unit cell, and Fig. 3a is the photo of the network for the specific configuration of charge -1 . The inset shows that there are four nodes represented by the cable connectors, labelled 1, 2, 3, 4 in each meta-atom. As such, there are four allowed subspaces. Each subspace can be characterized by a pseudo-angular momentum with $\exp(i4\varphi_n) = 1$ ($n = 1, 2, 3, 4$) (ref. ²⁸), with $\varphi_1 = 0$, $\varphi_2 = \pi/2$, $\varphi_3 = \pi$ and $\varphi_4 = -\pi/2$. In the experiment, we work with the subspace $\varphi_2 = \pi/2$ to realize our 3×3 real Hamiltonian (equation (2)), wherein the eigenfunctions

in the four nodes have relative phases of $1, i, -1$ and $-i$). The meta-atoms were connected to the next unit cell by 2-m-long coaxial cables (model RG58C/U, Belden) to realize the complex hoppings by braiding (Fig. 3b, see Supplementary Information section IX)^{28,29}. Both the amplitude and phase of the voltage of each meta-atom are monitored by an oscilloscope (see detailed experiment methods in Supplementary Information section IX and Supplementary Fig. 25). After Fourier transformation, we obtain the eigenstate distributions in the momentum space. The bandstructure and eigenstates corresponding to each non-Abelian topological charge can then be mapped experimentally. Figure 3c–j shows the experiment results (right panels), which agree well with the tight-binding model results on the left panels. The experiment parameters for each case are summarized in Supplementary Table 2 (see Supplementary Fig. 24 for corresponding network connectivity). The insets in Fig. 3c–j show the measured edge state distributions in the corresponding bandgaps with the theoretical results shown on the left for comparison. Taking the charge $+i$ configuration for example, a peak is observed in the bandgap between the second and third bands. The theoretical field distributions of the edge states are shown in Supplementary Fig. 5 for reference (see Supplementary Information section III). Most edge states in Fig. 3c–j can be well understood according to the analysis in Fig. 2. We note that the edge states of charge $+j$ in Fig. 3e do not appear as BICs, as shown in Fig. 2c. As mentioned above, the presence of BICs is special to the flatband situation where the second band states are decoupled from the two winding states, whereas in general cases (as in the experiment), the edge states are located both in the first and second bandgaps for the charge of $+j$ (see details in Supplementary Information section III and Supplementary Fig. 6). In addition, the edge states for the charge of -1 are fickle, as expected. The formation of edge states can be visualized by extending the 1D Hamiltonian onto a two-dimensional (2D) extended plane, where the edge states of the 1D system are inherently related to the topological degeneracy points encircled by the 1D Hamiltonian (see details in Supplementary Information section VII and Supplementary Figs. 15–19).

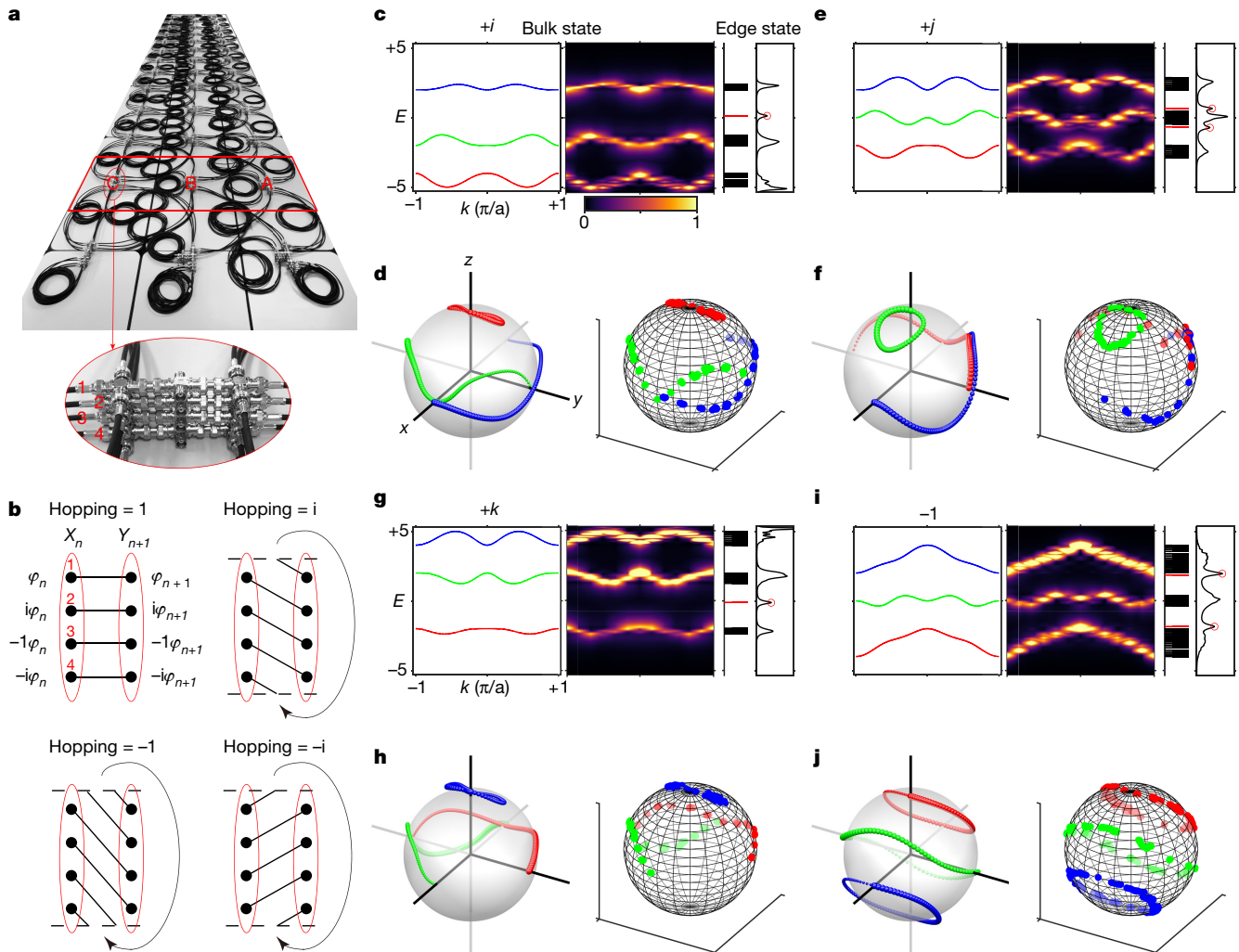


Fig. 3 | Experimental characterization of non-Abelian topological charges and hard boundary edge states. **a**, A sample photo of transmission line network, where 13 periods are used in the construction. The inset shows each meta-atom, consisting of four nodes stacked perpendicularly. **b**, Realization of complex-number hoppings between meta-atoms X_n and Y_{n+1} with X or $Y = A, B, C$. **c, e, g, i**, Theoretically simulated (left panels) and experimentally mapped (right panels) bulk states for $+i$ (**c**), $+j$ (**e**), $+k$ (**g**) and -1 (**i**). The projected edge

states are shown in the corresponding insets. **d, f, h, j**, Theoretically simulated (left panels) and experimentally mapped (right panels) eigenstate frame spheres for $+i$ (**d**), $+j$ (**f**), $+k$ (**h**) and -1 (**j**). The first, second and third bands are coloured as red, green and blue, respectively. The direction of decreasing line width indicates $k = -\pi/a \rightarrow \pi/a$, where $a = 1$. The parameters for all cases (**c–j**) are shown in Supplementary Table 2 (see Supplementary Information section III).

Here the edge states in Fig. 3*i* are due to a linear triple degeneracy in the 2D extended plane (Supplementary Fig. 16d).

Non-Abelian quotient relation

When two semi-infinite lattices carrying different non-Abelian topological charges meet at a domain wall—for example, forming the charge pair of $(+i, +j)$ —some domain-wall states should emerge. The well known Abelian bulk–edge correspondence, given by the difference of two integers (Fig. 4a, $\Delta N = N_L - N_R \in \mathbb{Z}$) becomes inadequate for describing the global edge-state configuration in non-Abelian topological systems. Here, we find a non-Abelian quotient relation as schematically shown in Fig. 4a, which states that the topology of the domain-wall is indicated by $\Delta Q = Q_L/Q_R$ ($Q_{L,R}, \Delta Q \in \mathbb{Q}$), also dubbed the ‘domain-wall charge’. Here we emphasize that a domain wall can be characterized by ΔQ in the presented models only thanks to the existence of a joint basepoint. From the perspective of group theory, the corresponding domain-wall topology of the Abelian ($\Delta N = N_L - N_R$) and non-Abelian ($\Delta Q = Q_L/Q_R$) systems is consistent, because both can be unified by multiplying the left charge by the inverse of the right charge. Our non-Abelian quotient

relation is hence an extension of the Abelian case. The domain-wall charge ΔQ can be related to the number as well as to the arrangement of edge states in each bandgap (see Fig. 4b).

In order to substantiate the non-Abelian quotient relation, we start from an Abelian perspective. As shown in Fig. 4c, two bandgaps are individually labelled by the corresponding Zak phases for each quaternion charge. The Zak phase for a single bandgap takes the value of 0 or π as the homotopy mapping $\pi_1[O(3)/(O(2) \times O(1))] = \pi_1(\mathbb{R}P^2) = \mathbb{Z}_2$, which means one cannot distinguish $+\pi$ from $-\pi$. Here in the multiple bandgap system, we use $+\pi$ and $-\pi$ to make the distinction between two conjugate elements in one conjugacy class. For example, we label the first (second) bandgap of charge $\pm i$ with 0 ($\pm \pi$) (as shown in Fig. 4c). This is because in each conjugacy class the two elements (for example, $+i$ and $-i$) have a relative meaning, that is, representing the two opposite rotations of the eigenstate frame when k runs across the first Brillouin zone ($k = -\pi \rightarrow \pi$). Between two different classes, the Zak phases $+\pi$ and $-\pi$ are topologically equivalent, consistent with the usual argument in the Abelian topological phases. As the class -1 goes beyond the Zak phase description¹⁶, we label it as 2π to make the distinction between it and the trivial class $+1$ (see description labelled by ‘**’ in the legend of Fig. 4).

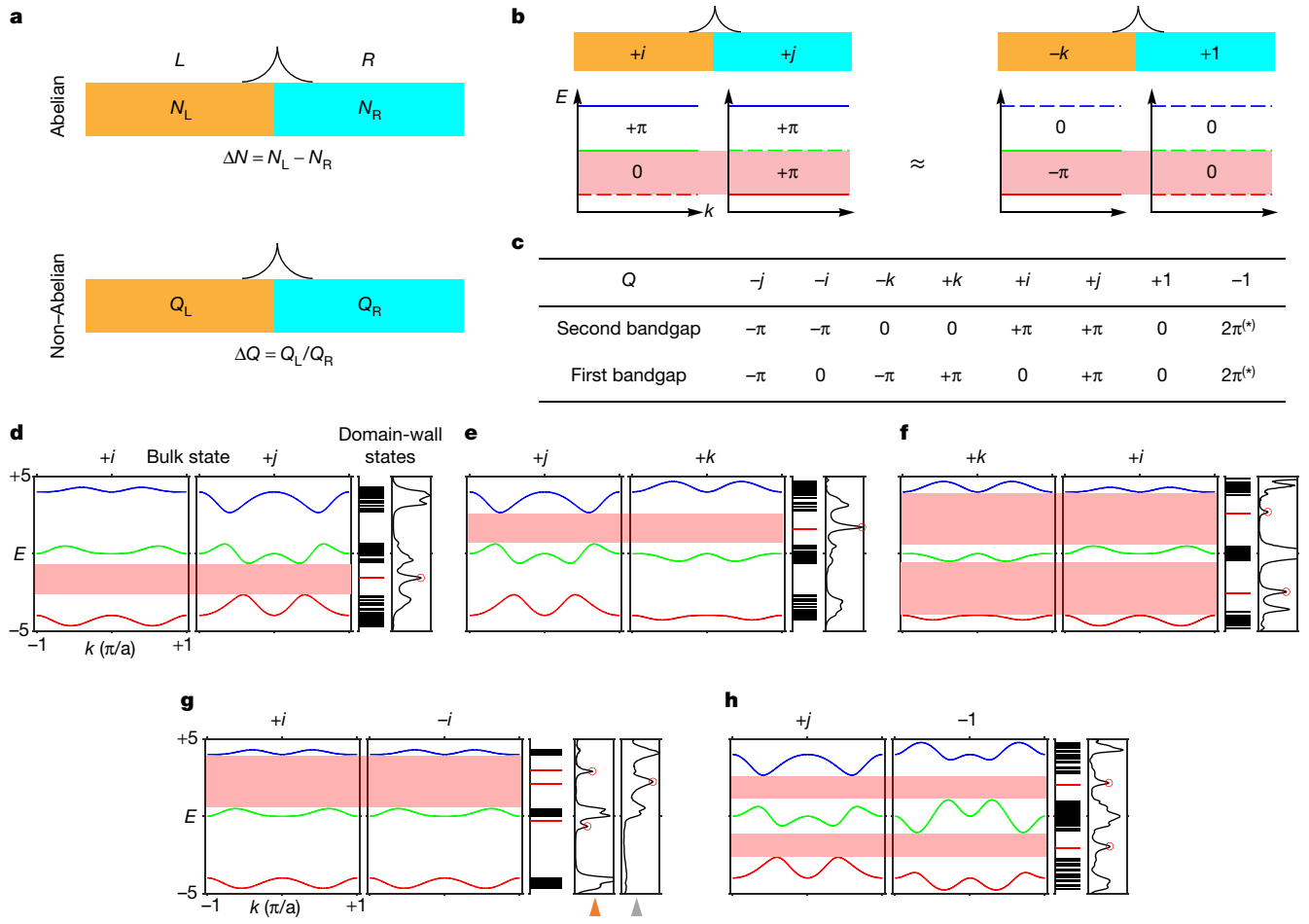


Fig. 4 | Non-Abelian quotient relation. **a**, Schematically illustrating the Abelian bulk–edge correspondence and non-Abelian quotient relation (domain-wall charge). L, left; R, right. The black traces represent the edge/ domain-wall states. **b**, Each bandgap is labelled by the corresponding Zak phase. The first bandgap carrying different Zak phases across the domain wall supports domain-wall states, as shaded in red. The domain-wall states are characterized by $\Delta Q = (+i)/(+j) \approx (-k)/(+1)$. The domain-wall states of the charge pair $(-k, +1)$ can be regarded as hard boundary edge states of charge $-k$. **c**, Non-Abelian topological charges are related to the Zak phases of both

bandgaps sandwiched by the three bands. *The charge -1 corresponds to the case that the eigenstate frame undergoes a rotation of 2π about an axis through the origin with an arbitrary orientation. The winding trajectories of the three eigenstates cannot be contractible simultaneously. **d–h**, Bulk states and domain-wall states between the two different non-Abelian topological charges labelled at the top of each panel. Left panels are simulations, right panels show experimental results. The domain-wall constructions are given in Supplementary Fig. 21. Colourful triangles in **g** indicate the results probed at the corresponding positions as shown in Supplementary Figs. 21, 22.

We next consider the existence of domain-wall states for each bandgap from a Zak phase perspective. As shown in Fig. 4b for the bandgap shaded in red, the Zak phases change across the domain wall, which implies the emergence of topological edge states in the first bandgap. In the second bandgap, there is no Zak phase change, and hence no edge state. Such a domain-wall state distribution is exactly the same as that when a system with charge of $\pm k$ (Fig. 2d) meets a hard boundary (charge $+1$). On the other hand, the global analysis based on the non-Abelian quotient relation shown in Fig. 4a, predicts that the number and position of domain-wall states for the charge pairs of $(+i, +j)$ and $(-k, +1)$ should be the same. This illustrates the non-Abelian quotient relation. One can apply similar arguments exhaustively for all other cases, which are all consistent with $\Delta Q = Q_L/Q_R$. As one can not specify the orientation of the domain wall, that means that the charge pairs of $(+i, +j)$ and $(+j, +i)$ share the same domain-wall state distributions. In total, there are five types of domain-wall state distributions, homomorphically corresponding to the five classes $(+1, \pm i, \pm j, \pm k, -1)$ in the quaternion group \mathbb{Q} . Going beyond this, we also provide a general argument of the non-Abelian quotient relation in Supplementary Information section VI (Supplementary Figs. 12–14).

In the experiment, we constructed several different types of domain walls (Supplementary Table 3 and Supplementary Fig. 21) and mapped

their domain-wall states accordingly, as shown in Fig. 4d–h. The experimental results agree with the theoretical predictions, further confirming the proposed non-Abelian quotient relation. In the domain wall of charge pair $(+i, -i)$, as shown in Fig. 4g, the domain-wall states share similar features with the hard boundary edge states of charge -1 (Supplementary Fig. 11d with $\theta_z \rightarrow 0$).

Discussion and outlook

In this work we avoid using the phrase ‘non-Abelian bulk–edge correspondence’ because the non-Abelian quotient relation $\Delta Q = Q_L/Q_R$ inherently depends on the existence of a basepoint. A robust bulk–edge correspondence that is meaningful even in the absence of a basepoint remains an open question for future investigations, such as only considering the conjugacy classes in the fundamental homotopy group or equivalently free homotopy classes of free loops.

The proposed ideas can be implemented in the optical regime, where coupled waveguides^{30–32} can support non-Abelian photonic states and even realize non-Abelian photon pumping in charge -1 by introducing spatial modulations along the waveguides³³. Other systems including dynamic optical lattices are also of interest³⁴.

Online content

Any methods, additional references, Nature Research reporting summaries, source data, extended data, supplementary information, acknowledgements, peer review information; details of author contributions and competing interests; and statements of data and code availability are available at <https://doi.org/10.1038/s41586-021-03521-3>.

1. Hasan, M. Z. & Kane, C. L. Topological insulators. *Rev. Mod. Phys.* **82**, 3045–3067 (2010).
2. Qi, X.-L. & Zhang, S.-C. Topological insulators and superconductors. *Rev. Mod. Phys.* **83**, 1057–1110 (2011).
3. Ando, Y. & Fu, L. Topological crystalline insulators and topological superconductors: from concepts to materials. *Annu. Rev. Condens. Matter Phys.* **6**, 361–381 (2015).
4. Kruthoff, J., de Boer, J., van Wezel, J., Kane, C. L. & Slager, R.-J. Topological classification of crystalline insulators through band structure combinatorics. *Phys. Rev. X* **7**, 041069 (2017).
5. Bradlyn, B. et al. Topological quantum chemistry. *Nature* **547**, 298–305 (2017).
6. Armitage, N. P., Mele, E. J. & Vishwanath, A. Weyl and Dirac semimetals in three-dimensional solids. *Rev. Mod. Phys.* **90**, 015001 (2018).
7. Ozawa, T. et al. Topological photonics. *Rev. Mod. Phys.* **91**, 015006 (2019).
8. Ma, G., Xiao, M. & Chan, C. T. Topological phases in acoustic and mechanical systems. *Nat. Rev. Phys.* **1**, 281–294 (2019).
9. Tang, F., Po, H. C., Vishwanath, A. & Wan, X. Comprehensive search for topological materials using symmetry indicators. *Nature* **566**, 486–489 (2019).
10. Zhang, T. et al. Catalogue of topological electronic materials. *Nature* **566**, 475–479 (2019).
11. Kim, M., Jacob, Z. & Rho, J. Recent advances in 2D, 3D and higher-order topological photonics. *Light Sci. Appl.* **9**, 130 (2020).
12. Schnyder, A. P., Ryu, S., Furusaki, A. & Ludwig, A. W. W. Classification of topological insulators and superconductors in three spatial dimensions. *Phys. Rev. B* **78**, 195125 (2008).
13. Kitaev, A. Periodic table for topological insulators and superconductors. *AIP Conf. Proc.* **1134**, 22–30 (2009).
14. Ryu, S., Schnyder, A. P., Furusaki, A. & Ludwig, A. W. W. Topological insulators and superconductors: tenfold way and dimensional hierarchy. *New J. Phys.* **12**, 065010 (2010).
15. Chiu, C.-K., Teo, J. C. Y., Schnyder, A. P. & Ryu, S. Classification of topological quantum matter with symmetries. *Rev. Mod. Phys.* **88**, 035005 (2016).
16. Wu, Q., Soluyanov, A. A. & Bzdušek, T. Non-Abelian band topology in noninteracting metals. *Science* **365**, 1273–1277 (2019).
17. Ahn, J., Park, S. & Yang, B.-J. Failure of Nielsen–Ninomiya theorem and fragile topology in two-dimensional systems with space-time inversion symmetry: application to twisted bilayer graphene at magic angle. *Phys. Rev. X* **9**, 021013 (2019).
18. Tiwari, A. & Bzdušek, T. Non-Abelian topology of nodal-line rings in PT-symmetric systems. *Phys. Rev. B* **101**, 195130 (2020).
19. Yang, E. et al. Observation of non-Abelian nodal links in photonics. *Phys. Rev. Lett.* **125**, 033901 (2020).
20. Bouhon, A. et al. Non-Abelian reciprocal braiding of Weyl points and its manifestation in ZrTe. *Nat. Phys.* **16**, 1137–1143 (2020).
21. Kang, J. & Vafek, O. Non-Abelian Dirac node braiding and near-degeneracy of correlated phases at odd integer filling in magic-angle twisted bilayer graphene. *Phys. Rev. B* **102**, 035161 (2020).
22. Jackiw, R. & Rebbi, C. Solitons with fermion number 1/2. *Phys. Rev. D* **13**, 3398–3409 (1976).
23. Hatsugai, Y. Chern number and edge states in the integer quantum Hall effect. *Phys. Rev. Lett.* **71**, 3697–3700 (1993).
24. Graf, G. M. & Porta, M. Bulk-edge correspondence for two-dimensional topological insulators. *Commun. Math. Phys.* **324**, 851–895 (2013).
25. Fang, C., Weng, H., Dai, X. & Fang, Z. Topological nodal line semimetals. *Chin. Phys. B* **25**, 117106 (2016).
26. Mermin, N. D. The topological theory of defects in ordered media. *Rev. Mod. Phys.* **51**, 591–648 (1979).
27. Basener, W. F. *Topology and Its Applications* 255–256 (Wiley, 2006).
28. Jiang, T. et al. Experimental demonstration of angular momentum-dependent topological transport using a transmission line network. *Nat. Commun.* **10**, 434 (2019).
29. Zhao, E. Topological circuits of inductors and capacitors. *Ann. Phys.* **399**, 289–313 (2018).
30. Rechtsman, M. C. et al. Photonic Floquet topological insulators. *Nature* **496**, 196–200 (2013).
31. Hafezi, M., Mittal, S., Fan, J., Migdall, A. & Taylor, J. M. Imaging topological edge states in silicon photonics. *Nat. Photon.* **7**, 1001–1005 (2013).
32. Dutt, A. et al. A single photonic cavity with two independent physical synthetic dimensions. *Science* **367**, 59–64 (2020).
33. Ke, Y. et al. Topological phase transitions and Thouless pumping of light in photonic waveguide arrays. *Laser Photonics Rev.* **10**, 1064 (2016).
34. Ünal, F. N., Bouhon, A. & Slager, R.-J. Topological Euler class as a dynamical observable in optical lattices. *Phys. Rev. Lett.* **125**, 053601 (2020).

Publisher's note Springer Nature remains neutral with regard to jurisdictional claims in published maps and institutional affiliations.

© The Author(s), under exclusive licence to Springer Nature Limited 2021

Data availability

The data and code that support the findings of this study are available in DataSpace@HKUST at <https://doi.org/10.14711/dataset/5LXMUZ>.

Acknowledgements This work is supported by the Hong Kong RGC (AoE/P-02/12, 16304717, 16310420) and the Hong Kong Scholars Program (XJ2019007). L.Z. acknowledges the National Natural Science Foundation of China (grant no. 12074230) and Shanxi Province 100-Plan Talent Program. S.Z. acknowledges support from the ERC Consolidator Grant (TOPOLOGICAL), the Royal Society and the Wolfson Foundation. C.T.C. thanks R. Cheng for making space available to construct the network.

Author contributions Q.G., B.Y., S.Z. and C.T.C. conceived the idea; T.J. designed the transmission line network with input from Z.-Q.Z. and C.T.C.; Q.G. and T.J. carried out all

measurements; Q.G., T.J., R.-Y.Z., Z.-Q.Z., B.Y., S.Z. and C.T.C. developed and carried out the theoretical analysis; L.Z. participated in the analysis and discussion of the results. B.Y., S.Z. and C.T.C. supervised the whole project. Q.G., T.J., R.-Y.Z. and B.Y. wrote the manuscript and the Supplementary Information with input from all other authors.

Competing interests The authors declare no competing interests.

Additional information

Supplementary information The online version contains supplementary material available at <https://doi.org/10.1038/s41586-021-03521-3>.

Correspondence and requests for materials should be addressed to B.Y., S.Z. or C.T.C.

Peer review information *Nature* thanks Xiang Ni, Baile Zhang and the other, anonymous, reviewer(s) for their contribution to the peer review of this work. Peer reviewer reports are available.

Reprints and permissions information is available at <http://www.nature.com/reprints>.